Published in "The European Physical Journal D 71(10): 262, 2017"
which should be cited to refer to this work.

Study of ^{3}He Rabi nutations by optically-pumped cesium magnetometers

Hans-Christian Koch[1,2,3,a], Georg Bison[3], Zoran Dragan Grujić[1], Werner Heil[2], Malgorzata Kasprzak[1,b], Paul Knowles[1,c], Andreas Kraft[2], Anatoly Pazgalev[5], Allard Schnabel[4], Jens Voigt[4], and Antoine Weis[1]

[1] Physics Department, University of Fribourg, 1700, Fribourg, Switzerland
[2] Department of Physics, Johannes Gutenberg-University, 55122 Mainz, Germany
[3] Paul Scherrer Institute, 5232 Villigen, Switzerland
[4] Physikalisch-Technische Bundesanstalt, Berlin, Germany
[5] Ioffe Physical Technical Institute, Russian Academy of Sciences, 194021 St. Petersburg, Russia

Abstract. We describe a method for recording the Rabi nutation of nuclear spin polarized ^{3}He by optically pumped cesium magnetometers. The measurement is performed by detecting the time-dependent magnetic field produced by the ^{3}He magnetization. The observed signals are compared to theoretical models and the results are used to precisely trace the evolution of the magnetization. This procedure represents a convenient way to control and measure the Rabi flip angle and the degree of spin polarization in experiments using ^{3}He magnetometers. The method requires only very coarse knowledge of the applied magnetic field's magnitude.

1 Introduction

Many of today's fundamental physics experiments require the precise and accurate measurement and tuning of an applied magnetic field. Atomic magnetometers are well suited for this task, since the (sensor volume averaged) frequency of the field-induced precession of the atomic spin polarization (at the Larmor frequency ω_L) is related to the magnetic field modulus by a constant, the gyromagnetic ratio $\gamma = \omega_L/|\boldsymbol{B}_0|$. An accurate field measurement thus calls for a precision frequency measurement combined with a precision knowledge of the gyromagnetic ratio. The nuclear spin of ^{3}He atoms is a proven candidate for magnetic field standards [1,2], since its gyromagnetic ratio γ_{He} is known to very high precision [3]. The precession frequency of ^{3}He can be measured indirectly in a non-perturbative manner through the detection of the rotating magnetic field produced by the precessing ^{3}He magnetization. Different methods can serve for this measurement, their applicability depends on the experimental circumstances. In strong magnetic fields and at high ^{3}He gas pressures, simple induction coils are efficiently used to detect the free spin precession (FSP) [4]. At low pressures of $\sim$1 mbar and weak magnetic fields of $\sim 1\,\mu$T the induced voltage ($\propto$ Larmor frequency, pressure) drops and a sensitive magnetometer, such as a superconducting quantum interference device (SQUID) [1] or an atomic magnetometer becomes the solution of choice [5]. The latter are advantageous in many applications since they are compact and operate at standard ambient temperatures.

Experiments searching for a permanent electric dipole moment of the neutron (nEDM) [6] require an accurate field control, for which ^{3}He magnetometers are well suited [7]. In that context the detection of the FSP of nuclear spin polarized ^{3}He gas by optically-pumped cesium magnetometers (CsOPMs) was recently demonstrated [8]. It was shown that, within restrictions imposed by the applied field's stability, the precision level of field measurements this type of magnetometer can achieve reaches the fundamental limit imposed by information theory, the so called Cramér-Rao-lower-bound [9]. Measurements of a $\sim 1\,\mu$T magnetic field with $\sim 5 \times 10^{-8}$ relative precision in 100 s integration time were reported. The sensitivity of the combined magnetometer concept was also theoretically investigated [10].

2 Measurement principle

A measurement with a ^{3}He-FSP magnetometer generally consists of three steps: optical pumping, spin flipping, and free-precession monitoring.

High degrees of nuclear polarization $p \sim 80\%$ can be conveniently achieved using metastable exchange optical pumping (MEOP) [11]. Pumping can be either done in situ, in the magnetometer vessel or ex situ using a suitable external polarizer unit [12]. Either process leaves the ^{3}He in the magnetometer vessel polarized along the direction of the applied magnetic field $\boldsymbol{B}_0 \parallel \boldsymbol{S}$. Since precession

[a] e-mail: kochhc@googlemail.com
[b] *Present address*: Instituut voor Kern- en Stralingsfysica, Katholieke Universiteit Leuven, 3001 Leuven, Belgium.
[c] *Present address*: LogrusData, Vienna, Austria.

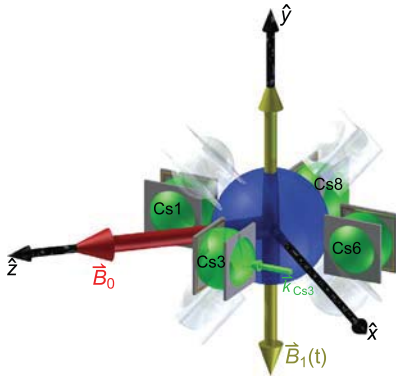

Fig. 1. Experimental geometry of the $Cs_\perp$ group. The ^{3}He cell (center sphere, blue) and the CsOPMs (smaller surrounding spheres, green) are shown. The holding field $\boldsymbol{B}_0$ points along $\hat{z}$ and the time dependent field $\boldsymbol{B}_1(t)$ used to flip the magnetization oscillates along $\hat{y}$. For the CsOPMs shown in this figure, the $\boldsymbol{k}_{Cs}$ of the Cs-D1 pump light is in the $\hat{x}$–$\hat{z}$ plane as indicated for Cs3 (small arrow, green). In each sensor $\boldsymbol{k}_{Cs}$ is perpendicular to the square plates around the Cs bulbs carrying the rf-coils. CsOPMs belonging to $Cs_\parallel$ are displayed as transparent spheres.

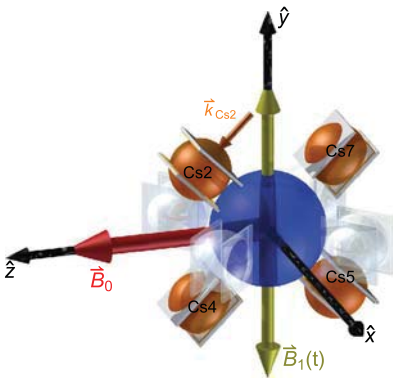

Fig. 2. Experimental geometry of $Cs_\parallel$ group (smaller surrounding spheres, orange). For the CsOPMs shown in this figure the $\boldsymbol{k}_{Cs}$ of the Cs-D1 pump light is in the $\hat{y}$–$\hat{z}$ plane as indicated for Cs2 (small arrow, orange). CsOPMs belonging to $Cs_\perp$ are displayed as transparent spheres.

only occurs when $\boldsymbol{S} \times \boldsymbol{B}_0 \neq 0$, either the spin polarization or the holding field has to be flipped to initiate the spin precession, and hence the magnetometer operation. Both methods have their respective merits and drawbacks. Flipping the field has the advantage that it can be done very reproducibly and the procedure is widely independent on the magnetic field conditions during the pumping. However, this approach is not possible when other parts of the experimental apparatus require the field to be at a fixed direction for operation. If, on the other hand, the spin is flipped, the holding field $\boldsymbol{B}_0$ remains static at all times, and a weak ($B_1 \ll B_0$) oscillating spin-flip field $\boldsymbol{B}_1(t) \perp \boldsymbol{B}_0$ is applied for a short time t_{flip}. The angle θ_{flip} by which the ^{3}He polarization is flipped then depends on the field magnitudes B_0 and B_1, the frequency ω_{sf} and the duration t_{flip}. Many experiments require a reproducible flip by a well defined angle θ_{flip}. The envisioned nEDM application calls for a $\pi/2$ flip with an accuracy on the level of $\Delta\theta_{\text{flip}} \approx 1\,\text{mrad}$ in order to minimize a systematic perturbation of the neutrons' precession created by a ^{3}He magnetization component along $\boldsymbol{B}_0$ [13]. For this reason it is important to precisely measure and tune the flipping angle. Below we will show that the combined ^{3}He/Cs magnetometer concept allows a high precision measurement of θ_{flip} during normal magnetometer operation, so that knowledge of the flip angle can be inferred without causing additional experimental effort.

3 The experimental apparatus

A detailed description of the ^{3}He/Cs magnetometer's design is given in references [8,10]. It consists of a $\sim$70 mm diameter spherical glass cell filled with $\sim$1 mbar of high purity ^{3}He gas. It is surrounded by eight CsOPMs, operated as laser-pumped double-resonance magnetometers in the M_x configuration [14]. Each CsOPM consists of a paraffin-coated spherical glass cell filled with cesium vapor that is traversed by a circularly polarized laser beam resonant with the Cs-D1 transition. The 895 nm light was produced by a commercial extended cavity diode laser system and delivered to each sensor via a multimode fiber. The power of the transmitted beam is measured by a photo-diode. Every CsOPM is further equipped with a pair of Helmholtz coils which produce a magnetic field oscillating at a constant frequency $\omega_{\text{rf,Cs}}$. This field drives a magnetic resonance in the vapor cell, which has the effect that the detected power acquires a component oscillating at the rf frequency $\omega_{\text{rf,Cs}}$. The amplitude and phase φ (of the photodiode signal with respect to the rf drive) of this oscillation depend on $\delta\omega_{\text{Cs}} = \omega_{\text{rf,Cs}} - \omega_{\text{L,Cs}}$. When $\omega_{\text{rf,Cs}} \approx \omega_{\text{L,Cs}}$, any small change ΔB_0 of the magnitude of the magnetic holding field will yield a small phase change $\Delta\varphi \propto \Delta B_0$. This phase is measured by demodulating the (transimpedance-amplified) photo-diode signal at $\omega_{\text{rf,Cs}}$ using a digital lock-in amplifier. The holding field applied for the experiments reported below was $B_0 \approx 1\,\mu\text{T}$, yielding Larmor frequencies of $\omega_{\text{L,Cs}}/(2\pi) \approx 3.5\,\text{kHz}$ and $\omega_{\text{L,He}}/(2\pi) \approx 32.4\,\text{Hz}$ for Cs and ^{3}He, respectively.

The CsOPMs are nominally located on cones around the $\boldsymbol{B}_0$ direction originating from the ^{3}He cell's center. By design the half-opening angles of these cones should be $\theta = 45°$, since at these positions the ^{3}He precession signal detected by the CsOPMs is maximized [8]. The nominal design distances of all CsOPMs from the ^{3}He cell-center are identical, $d = 50\,\text{mm}$. Deviations of the real setup from design and effects thereof on the measurement data will be addressed in detail in Section 4.2.

For reasons detailed in Section 4.4 it is reasonable to further distinguish two groups of CsOPMs. For the first group, that we refer to as $Cs_\perp$ group, the propagation direction of the Cs pump light $\boldsymbol{k}_{\text{Cs}}$ lies in the $\hat{x}$–$\hat{z}$ plane (cf. Fig. 1). For the second group, referred to as $Cs_\parallel$ group, the $\boldsymbol{k}_{\text{Cs}}$-vectors lie in the $\hat{y}$–$\hat{z}$ plane (cf. Fig. 2). The angular coordinates (θ_i, ϕ_i) of all magnetometers (in standard spherical coordinates) and the group they are associated with are summarized in Table 1.

$$\hat{\boldsymbol{\mu}}(t) = \frac{1}{\Omega^2}\begin{pmatrix} -\omega_1\delta\omega(1-\cos\Omega t)\sin\omega_{\rm sf}t + \omega_1\Omega\sin\Omega t\cos\omega_{\rm sf}t \\ \omega_1\delta\omega(1-\cos\Omega t)\cos\omega_{\rm sf}t + \omega_1\Omega\sin\Omega t\sin\omega_{\rm sf}t \\ \delta\omega^2+\omega_1^2\cos\Omega t \end{pmatrix}, \tag{1}$$

Table 1. Angular coordinates of CsOPMs. The values $\delta\theta$ refer to mechanical design uncertainties shown in Figure 4.

CsOPM	Group	θ_i	ϕ_i
Cs1	$\perp$	$\pi/4+\delta\theta$	π
Cs3	$\perp$	$\pi/4+\delta\theta$	0
Cs6	$\perp$	$3\pi/4-\delta\theta$	0
Cs8	$\perp$	$3\pi/4-\delta\theta$	π
Cs2	$\parallel$	$\pi/4+\delta\theta$	$\pi/2$
Cs4	$\parallel$	$\pi/4+\delta\theta$	$3\pi/2$
Cs5	$\parallel$	$3\pi/4-\delta\theta$	$3\pi/2$
Cs7	$\parallel$	$3\pi/4-\delta\theta$	$\pi/2$

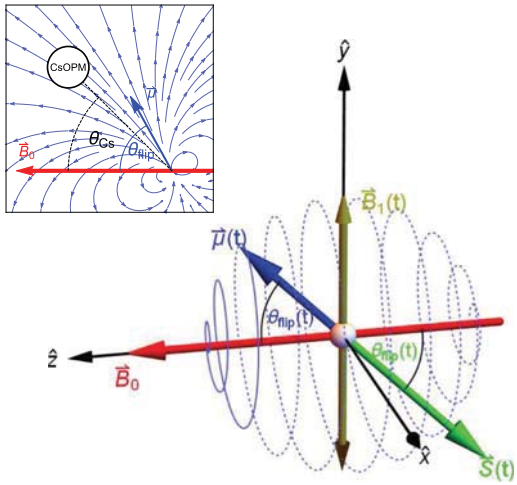

Fig. 3. The magnetization of the ^{3}He sample is initially aligned with $\hat{B}_0$ and evolves under the influence of the applied static and oscillating fields on the sphere indicated by the dashed line. Precession (fast) is occurring in the $\hat{x}$–$\hat{y}$ plane while nutation (slow) causes the time dependence of the flipping angle $\theta_{\rm flip}(t)$ which can be either understood as the angle between the magnetization $\boldsymbol{\mu}(t)$ and $\hat{B}_0$, or equivalently between the spin polarization vector $\boldsymbol{S}(t)$ and the negative $\hat{B}_0$ direction. The inset shows the magnetic dipole field created by the ^{3}He magnetization in the $\hat{z}$-$\hat{y}$ plane for a fixed moment in time when $\boldsymbol{\mu}$ lies in that plane. The CsOPM, located in the same plane under the angle $\theta_{\rm Cs}$ with respect to $\hat{B}_0$, measures (to first order) the projection of the dipole field at its position onto the $\hat{B}_0$ direction.

4 Signal modeling

In our previous publications [8,10] we have described how the magnitude $B_0 = |\boldsymbol{B}_0|$ of the applied magnetic holding field can be inferred from the ^{3}He-FSP signal. Here we focus on the time period preceding the FSP proper, during which the ^{3}He spins are flipped by an oscillating magnetic field.

The CsOPMs do, of course, also monitor the ^{3}He spin dynamics during this spin-flip phase. In order to model the expected signals, we first calculate the time evolution of a magnetic moment $\boldsymbol{\mu}(t)$ exposed simultaneously to a static holding field $\boldsymbol{B}_0 = B_0\hat{z}$ and an oscillating orthogonal magnetic field $\boldsymbol{B}_1(t) = 2B_1\cos(\omega_{\rm sf}t)\hat{y}$. We consider the dynamics in a coordinate frame that rotates around $\hat{z}$ at the angular frequency $\omega_{\rm sf}$ and apply the rotating wave approximation, yielding an effective field with components $(0, B_1, B_0 - \omega_{\rm sf}/\gamma_{\rm He})$. We solve the Bloch equations and the solution in the laboratory frame are obtained by an inverse rotation. Since the decay of the ^{3}He's spin polarization is very slow in sufficiently homogeneous magnetic fields we neglect relaxation effects on the typical timescale (tens of seconds) of the spin flip duration. Assuming a magnetic moment initially oriented along $\hat{z}$ and defining the detuning $\delta\omega = \omega_{L,\rm He} - \omega_{\rm sf}$, the magnetic moment's orientation evolves according to

see equation (1) above

where we have introduced the ^{3}He Rabi nutation frequency

$$\omega_1 = \gamma_{\rm He}B_1, \tag{2}$$

and the effective Rabi nutation frequency

$$\Omega \equiv \sqrt{\delta\omega^2+\omega_1^2}. \tag{3}$$

Equation (1) describes the evolution of $\boldsymbol{\mu}$ on a sphere.

The CsOPMs will detect the magnetic field produced by the ^{3}He magnetization. The magnetic far field produced by a 100% nuclear spin polarized gas of $N_{\rm He}$ atoms contained in a spherical volume centered at the origin is given by

$$\boldsymbol{B}_{\rm He}(\boldsymbol{r}) = \frac{\mu_0\mu_{\rm He}}{4\pi}N_{\rm He}\frac{3\boldsymbol{r}(\hat{\boldsymbol{\mu}}\cdot\boldsymbol{r}) - \hat{\boldsymbol{\mu}}\,|\boldsymbol{r}|^2}{|\boldsymbol{r}|^5}, \tag{4}$$

where $\mu_{\rm He}$ is the ^{3}He nuclear magnetic moment.

A quick estimation shows, that for a gas pressure of 1 mbar the field in close vicinity of the ^{3}He cell is on the order of pT. Combining equations (1) and (4) yields the time dependent magnetic field

$$\boldsymbol{B}_{\rm He}(t) \equiv \boldsymbol{B}_{\rm He}[\hat{\boldsymbol{\mu}}(t)], \tag{5}$$

produced by the ^{3}He magnetization which evolves under the influence of the static and oscillating fields. Based on equation (5) we now model the actual signal of a CsOPM

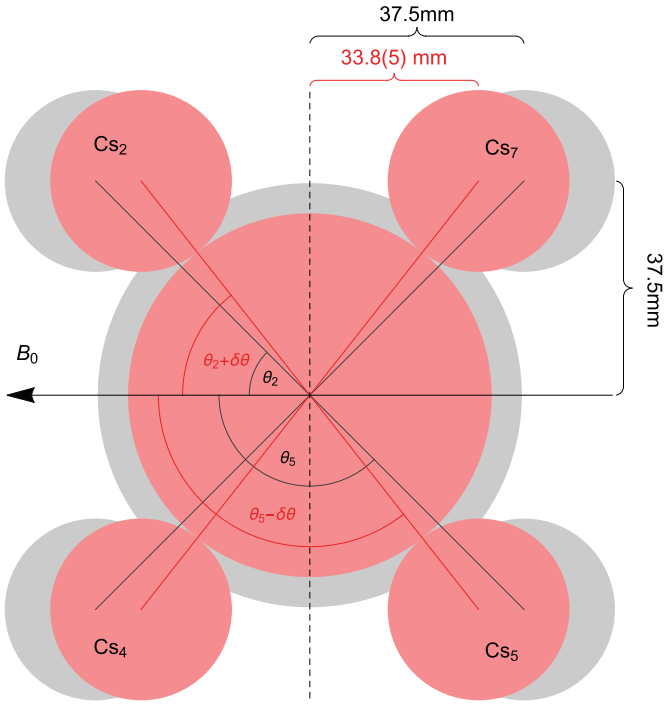

Fig. 4. Schematic cut through the apparatus along the $\hat{y}$–$\hat{z}$ plane (not to scale, compare Fig. 2). The apparatus consists of two halves fixed with respect to each other along the plane indicated by the dashed line. The design positions and real position are shown in gray and red, respectively. The reduced distance between the two halves implies errors on the θ_i angles, as illustrated for Cs2 and Cs5.

detecting this time-dependent magnetic field. Qualitatively, the expected signals can be deduced by simple reasoning (compare also Figs. 3 and 5, top row). In the beginning of the measurement the ^{3}He is magnetized along $\boldsymbol{B}_0$. No precession occurs, but the static field produced by the ^{3}He sample adds to the holding field at the CsOPM's position. When the flip-field is switched on, the ^{3}He magnetization is gradually driven out of the $\boldsymbol{B}_0$ direction, and the transverse components of the magnetization precess, leading to an oscillating magnetic field at the CsOPM's position. This oscillation gains in amplitude the further the magnetization is flipped and reaches its maximum at a flip angle of $\pi/2$, at this point the static component of the field created by the ^{3}He magnetization vanishes. From there on the oscillation amplitude decreases again until the flip angle reaches π, at the same time a static component with reversed sign builds up. When the magnetization has completely reversed direction the oscillation vanishes (no precession) and the magnitude of the static component is maximal again.

In practice, when these fields are detected by a CsOPM, a number of additional effects have to be taken into account to correctly interpret the observed signals. In the following we list all effects that we have considered and that are included in the final expression which is then used to fit the experimental data.

4.1 Vector component magnetometry

By virtue of their operating principle, the CsOPMs are scalar magnetometers, that measure the modulus $|\boldsymbol{B}_0 + \boldsymbol{B}_{\mathrm{He}}|$ of the total magnetic field averaged over the Cs-cell volume. Since the field created by the precessing ^{3}He magnetization is much smaller than the holding field ($B_{\mathrm{He}} \ll B_0$), a Taylor expansion of the last expression shows that the CsOPMs are, to first order, only sensitive to the component, $B_{\mathrm{He,z}}(t)$, of $\boldsymbol{B}_{\mathrm{He}}(t)$ along the holding field $\boldsymbol{B}_0$. Assuming that the oscillating field $\boldsymbol{B}_1(t)$ is switched on at time $t = 0$, the detected vector component of the ^{3}He field is thus given by

$$\begin{aligned} B_{\mathrm{He,z}}(t) &= \boldsymbol{B}_{\mathrm{He}}(t) \cdot \hat{\boldsymbol{B}}_0 \\ &= \frac{N_{\mathrm{He}}\mu_{\mathrm{He}}\mu_0}{8\pi d^3 \Omega^2}[(1+3\cos 2\theta)\left(\omega_1^2 \cos \Omega t + \delta\omega^2\right) \\ &\quad + 3\omega_1 \sin 2\theta\{\Omega \cos(\omega_{\mathrm{sf}} t - \phi) \sin \Omega t \\ &\quad + \delta\omega(\cos \Omega t - 1)\sin(\omega_{\mathrm{sf}} t - \phi)\}]. \end{aligned} \tag{6}$$

Here d, θ, and ϕ are the spherical coordinates of any given Cs-sensor cell. Evaluating equation (6) explicitly for the coordinates (d, θ_i, ϕ_i) of each CsOPM, Cs_i ($i = 1, \ldots, 8$), yields eight expressions $B^{(i)}_{\mathrm{He,z}}(t)$ that describe the expected z-components of the magnetic field at the sensor positions.

4.2 Mechanical imperfections and degree of polarization

Due to mechanical imperfections, the real apparatus may deviate from its design geometry, e.g., the radial and angular positions of the CsOPMs, which will affect the measurement data. Equation (4) shows that the strength of the magnetic (dipole) field created by the ^{3}He sample drops with $1/d^3$. As a result the amplitude of the observed oscillation signal is very sensitive to the spacing, $d^{(i)}$, between ith CsOPM and the ^{3}He cell. The amplitude of the signal further depends on the degree of spin polarization P_{He} of the gas sample which is not known a priori. We take both effects into account by introducing an effective distance parameter

$$\left(d'^{(i)}\right)^3 = \frac{\left(d^{(i)}\right)^3}{P_{\mathrm{He}}}, \tag{7}$$

in the model.

The dependence of the signal on the angular coordinates is more delicate, as we can see from equation (6). The $\phi^{(i)}$ coordinate produces a phase shift between ^{3}He FSP-signals measured on different sensors, an effect which can be exploited in the context of common-mode noise suppression (CMNR) [8]. Slight deviations of the $\phi^{(i)}$ coordinates from their design values may affect the CMNR but their influence on the measurement data remains restricted to the abovementioned phase shift which will not hamper the analysis.

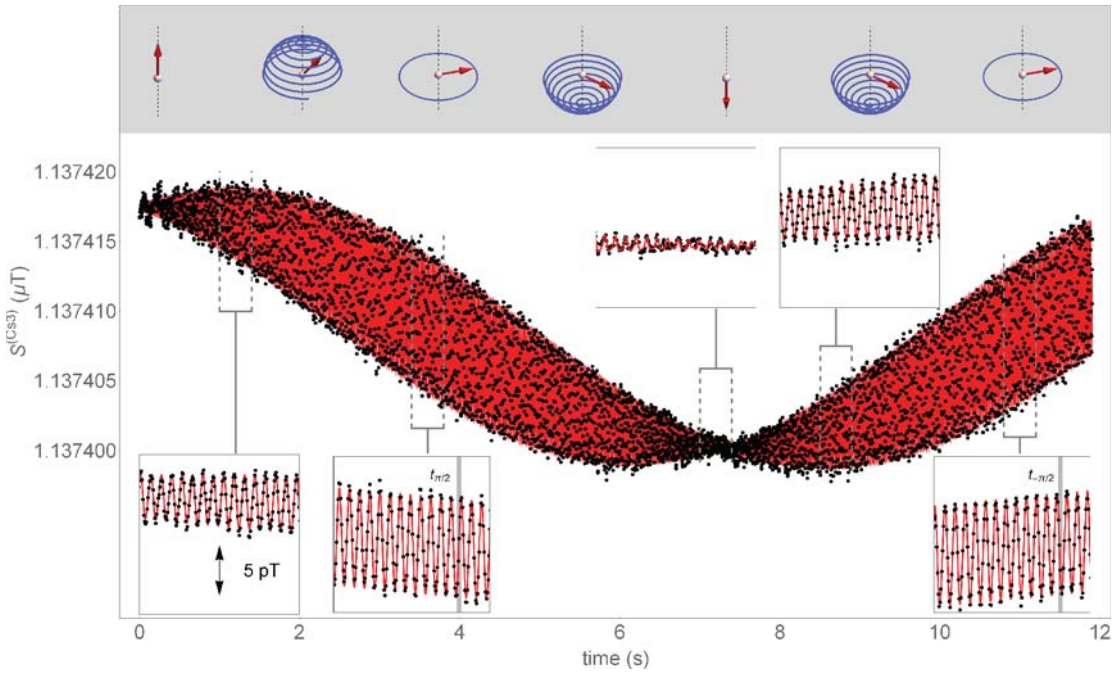

Fig. 5. Time series of magnetometer Cs3 data (black dots, foreground), and fit (red, background). The rectangular insets show closeups on the data at the positions specified by the dashed lines. The times at which an exact $\pi/2$-flip has occurred are shown as solid vertical lines in the second and rightmost closeup. The upper row illustrates the trajectory of the ^{3}He's Bloch vector during the flipping.

Deviations of the $\theta^{(i)}$ coordinates from design, on the other hand, cannot be neglected. The combined ^{3}He/Cs magnetometer is assembled from two symmetric halves, one comprising the sensors Cs1–Cs4, and the other one the sensors Cs5–Cs8, the $\hat{x}$–$\hat{y}$ plane being shared by the two assembled halves. In the measurements described here, the spacing between the two halves was slightly smaller than its design value because a smaller-than-design ^{3}He cell was used and priority was given to minimizing the distance between the ^{3}He cell and the CsOPMs. Figure 4 illustrates this geometrical mismatch which implies a considerable deviation of the $\theta^{(i)}$ coordinates from their design values $\widetilde{\theta}^{(i)}$. Based on coordinate measurements (compare Tab. 1) of the assembled apparatus we estimate the average deviation to be $\delta\theta = |\widetilde{\theta} - \theta| \approx 3.0(4)^\circ$. To take this effect into account, the $\theta^{(i)}$ angle will be a free parameter in the fit function to be defined in Section 4.6 and its exact value will be inferred by the fit routine.

4.3 Bandwidth limitation

To correctly model the expected signals another important property of the CsOPM has to be taken into account. As discussed, e.g., in [15] the response of the CsOPM exhibits a first order low-pass characteristic in the fixed-frequency mode of operation which applies here. The transfer function of this low-pass is given by

$$T(f)^{(i)} = \sqrt{\frac{1}{1 + (2\pi f\, \tau^{(i)})^2}}, \tag{8}$$

where $\tau^{(i)} = 1/\Gamma_2^{(i)}$ is the lifetime and $\Gamma_2^{(i)}$ the transverse relaxation rate of the cesium polarization in the cell of the ith CsOPM. The -3 dB cut-off frequency $f_{3\mathrm{dB}}$ of this filter is typically $\approx$5 Hz for the CsOPMs used in this study [16]. Inspection of equation (6) reveals components oscillating at frequencies $\omega_{\mathrm{sf}} \approx \omega_{L,\mathrm{He}} \approx (2\pi)37$ Hz and $\sqrt{(\omega_{L,\mathrm{He}} - \omega_{\mathrm{sf}})^2 + \omega_1^2} \approx \omega_1$. The measured amplitude of the component oscillating at ω_{sf} will be significantly reduced by the atomic low-pass filter (LPF) effect. However, for a weak flipping field ($B_1 \ll B_0$), the Rabi frequency $\omega_1 \approx 100$ mHz is very slow compared to the Larmor frequency and its amplitude is virtually not affected by the atomic LPF. We take this effect into account by introducing, in equation (6), transmission factors $T^{(i)}(\omega_{\mathrm{sf}}) \equiv T^{(i)}$, in front of all terms oscillating at ω_{sf}, i.e., by making the replacements

$$\cos(\omega_{\mathrm{sf}} t - \phi^{(i)}) \quad \Rightarrow \quad T^{(i)} \cos(\omega_{\mathrm{sf}} t - \phi^{(i)}), \tag{9}$$

and

$$\sin(\omega_{\mathrm{sf}} t - \phi^{(i)}) \quad \Rightarrow \quad T^{(i)} \sin(\omega_{\mathrm{sf}} t - \phi^{(i)}). \tag{10}$$

4.4 Parasitic detection of the rf spin-flip field

The CsOPM signals are also affected by the applied $\boldsymbol{B}_1(t)$ field and may acquire components oscillating at ω_{sf} and $2\omega_{\mathrm{sf}}$. The ω_{sf} component arises from a nonzero projection of the $\boldsymbol{B}_1(t)$ field on the $\hat{B}_0$ direction at the CsOPM's position which may occur due to a misalignment or inhomogeneities of the two fields. The $2\omega_{\mathrm{sf}}$ component can be explained by the fact that the CsOPM measures the

Table 2. Individual pick-up amplitudes obtained in calibration measurement. For Cs7 the amplitude could not be determined due to a DAQ problem. The values in brackets are inferred by the fit of the real measurement data described in Section 6.

CsOPM	Group	$B'^{(i)}_{1\omega}$(pT)	$B'^{(i)}_{2\omega}$(pT)
Cs1	$\perp$	0.63	0.19
Cs3	$\perp$	0.13	0.19
Cs6	$\perp$	1.42	0.31
Cs8	$\perp$	1.90	0.31
Cs2	$\parallel$	7.31	0.28
Cs4	$\parallel$	6.82	0.23
Cs5	$\parallel$	6.53	0.24
Cs7	$\parallel$	(6.75)	(0.24)

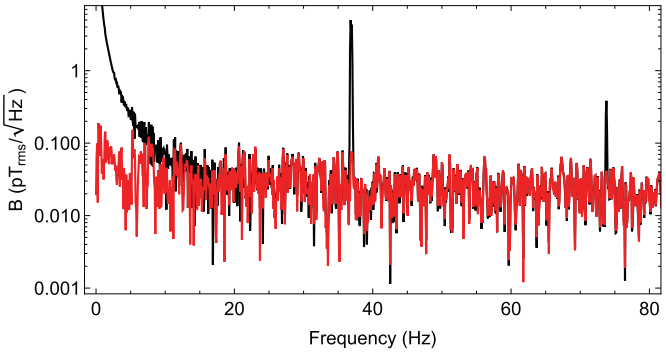

Fig. 6. FFT spectra of the CsOPM signal (black, background) and the fit residuals (red, foreground) of magnetometer Cs3. The full dataset was used to calculate the spectrum.

modulus of the total magnetic field, by virtue of which a component of $\boldsymbol{B}_1(t)$ oscillating at $\omega_{\rm sf}$ that is transverse to $\boldsymbol{B}_0$ will produce a $2\omega_{\rm sf}$ component. In order to quantitatively assess this pick-up effect for each individual CsOPM, a calibration measurement was performed during which the CsOPMs were exposed to the same oscillating $\boldsymbol{B}_1(t)$ field that was later used for actual data taking, but the ^{3}He being unpolarized. The pick-up amplitudes were inferred by fits of a function $B'^{(i)}_{1\omega}\sin(\omega_{\rm sf}t+\phi^{(i)}_{1\omega})+B'^{(i)}_{2\omega}\sin(2\omega_{\rm sf}t+\phi^{(i)}_{2\omega})$ to these data and are displayed in Table 2. It can be seen that the magnetometers of Cs$_\parallel$ systematically measure a larger oscillation amplitude $B'^{(i)}_{1\omega}$ compared to those of Cs$_\perp$ which motivates the distinction of the two groups made in Section 3. The reason for this distinct difference is most likely to be sought in inhomogeneities of the $\boldsymbol{B}_0$ and $\boldsymbol{B}_1(t)$ fields produced by Helmholtz coils wound around the $\hat{z}$ and $\hat{y}$ direction respectively. The geometry of the inhomogeneities expected in such a system qualitatively explains a systematically increased pick-up amplitude for the $Cs_\parallel$ group as compared to the $Cs_\perp$ group.

We take the pick-up effects into account by adding a phase-shifted oscillatory term $B'^{(i)}_{1\omega}\sin(\omega_{\rm sf}t+\phi^{(i)}_{1\omega}+\phi^{(i)}_0)+B'^{(i)}_{2\omega}\sin(2\omega_{\rm sf}t+\phi^{(i)}_{2\omega}+\phi^{(i)}_0)$ in the model expression for the ith CsOPM signal. For Cs7 the calibration measurement failed due to an unresolved DAQ problem. In the fits of this CsOPM's signals, $B'^{(7)}_{1\omega}$ and $B'^{(7)}_{2\omega}$ therefore remained free parameters. When the initial values of these fit parameters are appropriately chosen, the fit converges with $B'^{(7)}_{1\omega}$ and $B'^{(7)}_{2\omega}$ parameter values that are comparable to the ones observed for the other members of the Cs$_\parallel$ group. The different magnitudes of the pick-up lead to qualitatively different shapes of the signals observed during the ^{3}He spin-flip that become apparent in Figures 7 and 8.

4.5 Holding field inhomogeneity

The ith CsOPM will detect the magnetic oscillation $B^{(i)}_{{\rm He,z}}(t)$ superposed on a constant background field given by the magnitude of $\boldsymbol{B}_0(\boldsymbol{r}_i)$ at its position. We account for possible field inhomogeneities by using $B^{(i)}_0=|\boldsymbol{B}_0(\boldsymbol{r}_i)|$ for the ith sensor as a free fit parameter.

4.6 Fit function

Taking all the above into account, the model expression for the time-dependent magnetic field $B^{(i)}_{\rm exp}(t)$ that is detected by the ith CsOPM during the ^{3}He spin-flip reads

$$\begin{aligned}B^{(i)}_{\rm exp}(t) = {}& B^{(i)}_0 + B'^{\,(i)}_{1\omega}\sin(\omega_{\rm sf}t+\phi^{(i)}_{1\omega}+\phi^{(i)}_0)\\ &+ B'^{\,(i)}_{2\omega}\sin(2\omega_{\rm sf}t+\phi^{(i)}_{2\omega}+\phi^{(i)}_0)\\ &+ \frac{N_{\rm He}\mu_{\rm He}\mu_0}{8\pi(d'^{(i)})^3\Omega^{(i)\,2}}\Big[\Big(1+3\cos 2\theta^{(i)}\Big)\\ &\times\Big(\omega_1^{(i)\,2}\cos\Omega^{(i)}t+\delta\omega^{(i)\,2}\Big)\\ &+3T^{(i)}\omega_1^{(i)}\sin 2\theta^{(i)}\Big\{\Omega^{(i)}\cos(\omega_{\rm sf}t-\phi^{(i)})\\ &\times\sin\Omega^{(i)}t+\delta\omega^{(i)}\Big(\cos\Omega^{(i)}t-1\Big)\\ &\times\sin(\omega_{\rm sf}t-\phi^{(i)})\Big\}\Big],\end{aligned}\tag{11}$$

which represents the fit function after substituting $\omega_1^{(i)}$ with equation (2), $\Omega^{(i)}$ with equation (3) and $\delta\omega^{(i)}=\omega^{(i)}_{\rm L,He}-\omega_{\rm sf}$. The quantities $T^{(i)}$, $B'^{\,(i)}_{1\omega}$, $B'^{\,(i)}_{2\omega}$, $\phi^{(i)}_{1\omega}$, $\phi^{(i)}_{2\omega}$, $\phi^{(i)}$ and $N_{\rm He}$, μ_0, $\mu_{\rm He}$, $\omega_{\rm sf}$ are predefined constants for each CsOPM and global constants for all fits, respectively. The quantities $d'^{(i)}, \omega^{(i)}_{\rm L,He}, B^{(i)}_0, \phi^{(i)}_0, B^{(i)}_1$ and $\theta^{(i)}$ are free parameters of the fits. As discussed in Section 4.2, the $\theta^{(i)}$ angle of the CsOPMs' positions deviates from the optimal geometry and is therefore included in the free parameter set and its exact value inferred by the fit routine. The fits of the experimental data presented in the following actually yield values $\delta\theta^{\rm mean(1-4)}=3.24(48)^\circ$ and $\delta\theta^{\rm mean(5-8)}=3.09(60)^\circ$ for the two halves of the magnetometer assembly, respectively. This process produces stable results which agree with the expectations arising from geometrical examinations of the apparatus.

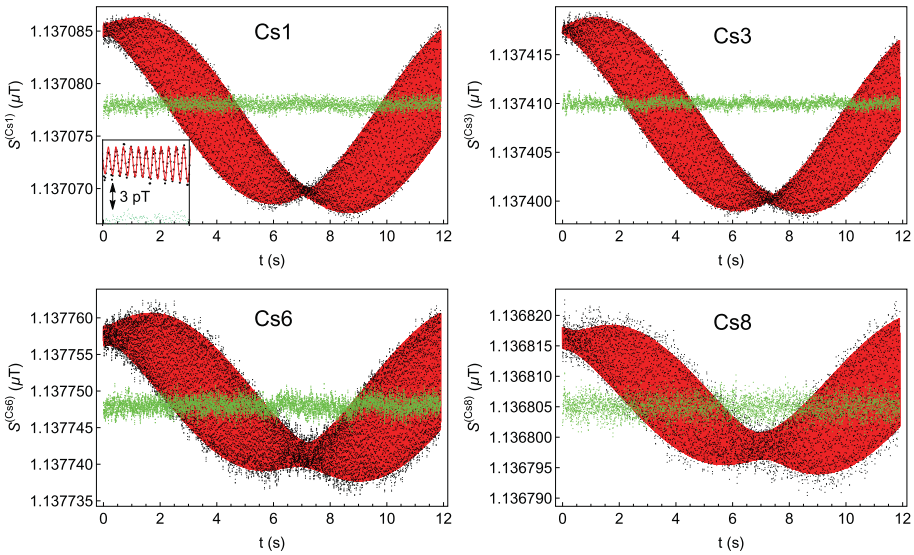

Fig. 7. Recorded time series (black points), fit function (red, background) and fit residuals (green, foreground) of signals from $Cs_\perp$ group magnetometers recorded during ^{3}He spin flip. Excellent quantitative agreement is found. The inset in the upper left graph shows a closeup on the data in the time interval $0.8\,\mathrm{s} < t < 1.1\,\mathrm{s}$ on a stretched timescale.

5 Method

The measurements presented in the following were performed inside the magnetically shielded room BMSR-2 of Physikalisch Technische Bundesanstalt, Berlin, one of the world's magnetically most quiet and stable environments. The magnetometer was immersed in a homogeneous magnetic field $\boldsymbol{B}_0 \parallel \hat{z}$ with $|\boldsymbol{B}_0| \approx 1\,\mu$T. Both, $\boldsymbol{B}_0$ and $\boldsymbol{B}_1(t)$ were produced by large Helmholtz coils [17]. Prior to polarizing the ^{3}He, the magnitude of the magnetic field at the ^{3}He cell-center was estimated. This was done by measuring the resonance frequencies of all eight CsOPMs and calculating their average $\omega_{\mathrm{L,Cs}}^{\mathrm{Mean}}$. Using the relation $\omega_{\mathrm{L,He}} \approx \omega_{\mathrm{L,Cs}}^{\mathrm{mean}} \gamma_{\mathrm{He}}/\gamma_{\mathrm{Cs}}$, the spin flip frequency ω_{sf} was chosen accordingly. A weak gas discharge was ignited in the magnetometer cell and the ^{3}He was nuclear spin polarized by MEOP [11] using a laser resonant with the C_9 transition. After the ^{3}He sample was polarized, the discharge and pump-laser were switched off. The sinusoidal oscillating spin-flip field $\boldsymbol{B}_1 \parallel \hat{y}$ with a $\sim$2 nT amplitude was switched on for $\sim$12 s using a square wave gated function generator and the CsOPM phase signals $\varphi^{(i)}(t)$ were recorded during the ^{3}He Rabi nutation. Recording was done at 14 bit resolution and 450 Hz sampling rate[1] using the built in logging functionality of the digital lockin amplifiers. All CsOPMs were driven at the same constant frequency $\omega_{\mathrm{rf,Cs}}$, and the phase data were scaled to magnetic units according to

$$S^{(i)}(t) = \frac{1}{\gamma_{\mathrm{Cs}}} \left(\omega_{\mathrm{rf,Cs}} - \frac{\Gamma_2^{(i)}}{\tan\left[\varphi^{(i)}(t) - \varphi_0^{(i)}\right]} \right), \qquad (12)$$

[1] For the sensor Cs6 the acquisition rate was 900 Hz due to an error in the settings of the DAQ system.

where $\varphi_0^{(i)}$ is a magnetometer-specific phase offset that was determined by a separate calibration measurement. Finally, equation (11) was used to fit the magnetometer data $S^{(i)}(t)$.

6 Results and discussion

In Figure 5 a discrete time series of Cs3 data (black dots) is shown, together with the fitted function (red solid line) given by equation (11), several selected sections are displayed on a stretched timescale. One sees a remarkable agreement between the data and the fit. Figure 6 shows the FFT spectrum of that time series (black, background), together with a spectrum of the fit residuals (red, foreground). A large DC component and prominent oscillations at ω_{sf} and $2\omega_{\mathrm{sf}}$ are clearly visible in the data. The spectrum of the residuals shows no structure, which further proves that the fit function adequately models the signal.

The data and fits of all 8 CsOPMs are shown in Figures 7 and 8 for the $Cs_\perp$ and $Cs_\parallel$ groups, respectively. The qualitative difference between the signals from $Cs_\perp$ and $Cs_\parallel$ is that for the latter the fast oscillation is more prominent at all times because of the larger oscillating $\boldsymbol{B}_1(t)$ field pick-up by those sensors. It can nonetheless be seen that equation (11) does adequately reproduce the observed behavior for both – qualitatively quite different – types of signals. In the following we will address a number of specific features and perform a more quantitative analysis of the results.

6.1 Holding field

From the fits we can extract different independent values of the magnetic holding field B_0.

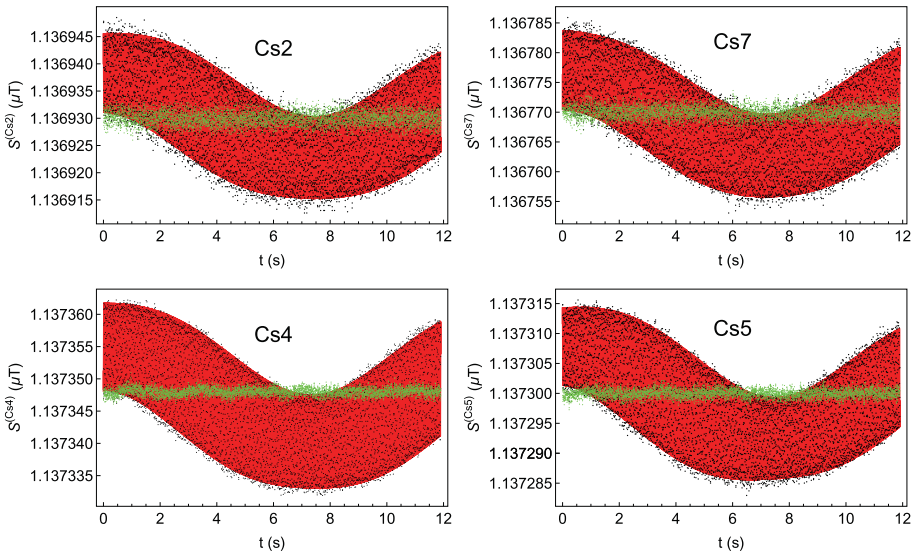

Fig. 8. Measurement data (black points), fit function (red, background) and fit residuals (green, foreground) of signals from $Cs_{\parallel}$ group magnetometers. The qualitative difference to Figure 7 is visible but the fit function adequately describes both cases.

– First, we get 8 values of the ^{3}He Larmor frequency from the 8 fit parameters $\omega^{(i)}_{\mathrm{L,He}}$, which are individually fit for each CsOPM. Since these are all simultaneous measurements of the **same** time-dependent field from the precessing ^{3}He magnetization – and thus represent the field in the center of the ^{3}He magnetometer cell [18] – we expect them to agree within their uncertainties. Inspection of the data shows that the parameter uncertainties calculated by the fit routine are too small to explain the scatter of the measured values. This underestimation of the experimental errors is to some extend expected since the fit routine will only produce realistic error estimates for a (flat) white Gaussian noise spectrum. In our case, however, the noise spectrum is deformed, e.g., due to the low-pass filter involved in the lock-in detection. To take this effect into account we upscale the uncertainties provided by of the fit routine by a common factor (∼6) to make them consistent with the observed scatter. The magnetic field values are calculated from $B_0 = \omega^{(i)}_{\mathrm{L,He}}/\gamma_{\mathrm{He}}$ and are shown, together with their weighted mean, in the left graph of Figure 9.
– Each fit also yields 8 values of the magnetic field from the fit parameters $B_0^{(i)}$ (= Cs Larmor frequencies) at the position of each of the 8 CsOPMs. These results are shown in the right graph of Figure 9 as blue dots and their mean is given by the upper (blue) line. The data from the left graph are repeated for convenience. Comparison shows that the two mean fields agree within ∼20 pT. Absolute equality is only expected in case of a perfectly homogeneous field, or in case where the field has only linear gradients. Any higher order field gradient or geometrical imperfection of the apparatus will result in deviations of the two means. Additional reasons for the inequality may be systematic errors of the inferred Cs Larmor frequencies ($\propto B_0^{(i)}$) due to Bloch–Siegert shifts, light shifts or errors of the initial phase settings [19].

6.2 Degree of polarization

The fits also yield the 8 effective distance parameters $d'^{(i)}$ introduced in Section 4.2, whose average value is

$$d'^{(\mathrm{mean})} = 55.3(1.8)\,\mathrm{mm}. \tag{13}$$

The uncertainty of the above value is caused by the scatter of the set of eight measurements, the individual uncertainties being much smaller (∼0.05 mm). Since all components of the magnetic field in equation (4) scale with μ/d^3, effects of increased CsOPM distance and reduced ^{3}He polarization are hard to distinguish. The apparatus is constructed such that the ^{3}He cell and the CsOPM cells actually touch, which assures that their (radial) spacings are in agreement with the design value. Variations of the distances between their individual centers may still occur due to the fact that the glass cells for ^{3}He and Cs are actually hand-crafted. Previous, independent measurements had suggested the presence of such deviations of ∼±1 mm [19] which agrees well with the spread found in equation (13). We use (13) to calculate the degree of polarization of the gas sample and find

$$P_{\mathrm{He}} = \left(\frac{d}{d'^{(\mathrm{mean})}}\right)^3 = 0.74(7). \tag{14}$$

This value is well in accordance with previous results, demonstrating the consistency of this method with earlier studies [10]. As noted above, the scatter of the cell distances dominates the error on the determination of the degree of polarization. We estimate that if the uncertainty on the (true) cell distance could be reduced to ∼0.1 mm, e.g., by the construction of a mechanically more precise

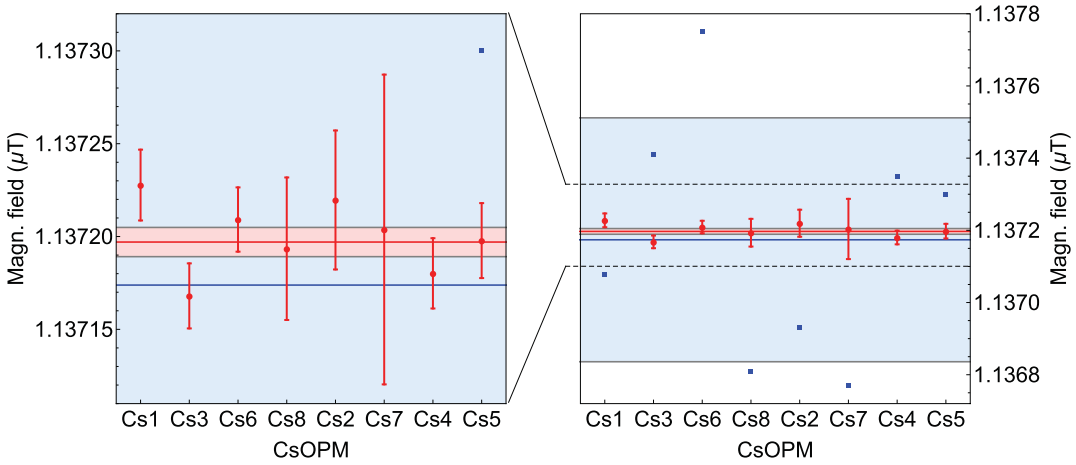

Fig. 9. Measurements of the holding field. *Left*: Holding field at the ^{3}He cell position calculated from the ^{3}He Larmor frequencies $\omega^{(i)}_{\mathrm{L,He}}$ (points with error bars) and their weighted mean (red horizontal line) with error band. *Right*: Values of $B^{(i)}_0$ at the centers of the Cs OPMs extracted from the fits (blue squares) together with their mean (blue line) and standard deviation (blue band). The $\omega^{(i)}_{\mathrm{L,He}}$ data from the left graph is also shown for comparison.

apparatus, this would allow determination of the degree of polarization with an uncertainty <1.

6.3 Rabi frequency and flip-angle

A central goal of the analysis presented in this paper was the precision prediction of the ^{3}He spin-flip angle's time dependence. The fit of each CsOPM signal produces one value $B^{(i)}_1$ and one value $\omega^{(i)}_{\mathrm{L,He}}$, thus yielding one value, $\Omega^{(i)}$, of the effective Rabi frequency. The measured Rabi frequencies for all eight CsOPMs are shown, together with their weighted mean, in Figure 10.

Using the relation

$$\theta^{(i)}_{\mathrm{flip}}(t) = \arccos(\mu^{(i)}_z(t)), \tag{15}$$

derived from equation (1) allows calculating $\theta^{(i)}_{\mathrm{flip}}$ for any given time t by inserting the fitted parameter values. The precision at which these parameters are known defines the precision of the θ_{flip} determination and scales inversely with the length of the calibration measurement. This dependency is shown in Figure 11, where the uncertainty of the calculated flip angle is plot as a function of measurement time. It can be seen that after the (arbitrarily chosen) flipping time of ∼11.9 s the uncertainty on the flip angle reaches the $\delta\theta_{\mathrm{flip}} \sim 4$ mrad level required for the nEDM application.

Assuming time-independent experimental conditions, one can use the result of a (long) calibration measurement to determine the appropriate flipping time needed to achieve any desired flipping angle. In many experimental situations one wishes to achieve a flip angle $\theta_{\mathrm{flip}} = \pi/2$ ('$\pi/2$-pulse'), e.g., to maximize the magnetometric sensitivity and minimize static field components created by a longitudinal ^{3}He magnetization along $\hat{z}$. The time at

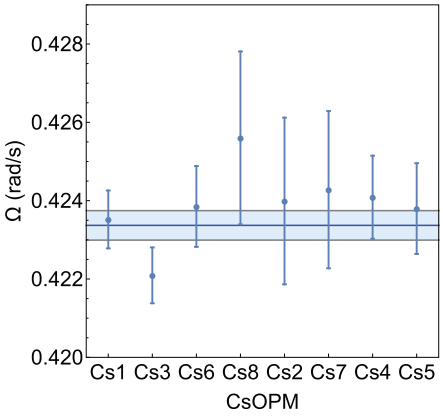

Fig. 10. Effective Rabi frequencies $\Omega^{(i)}$ of the ^{3}He spin flip as measured simultaneously by the eight CsOPMs. The horizontal blue line and band represent their weighted mean and its uncertainty $\Omega^{(\mathrm{mean})} = 0.4234(4)$ rad/s.

which $\theta_{\mathrm{flip}} = \pm\pi/2$ is reached[2] can be found by solving $\mu^{(i)}_z(t_{\pm\pi/2}) = 0$ in equation (1), yielding

$$t_{\pi/2} = \pm\frac{\arccos(-\delta\omega^2/\omega_1^2) + 2n\pi}{\Omega}, \tag{16}$$

with $n \in \{0, 1, 2, 3, 4, \ldots\}$. The smallest (positive) times for which this condition is fulfilled are

$$t_{\pi/2} = +\frac{\arccos(-\delta\omega^2/\omega_1^2)}{\Omega} \quad \text{for} \quad \theta_{\mathrm{flip}} = +\pi/2, \tag{17}$$

[2] We note that we use the nomenclature $+\pi/2$ and $-\pi/2$ to identify the cases in which the condition $\theta_{\mathrm{flip}} = \pi/2$ is approached from smaller (e.g., first occurence) and larger (e.g., second occurence) angles, respectively.

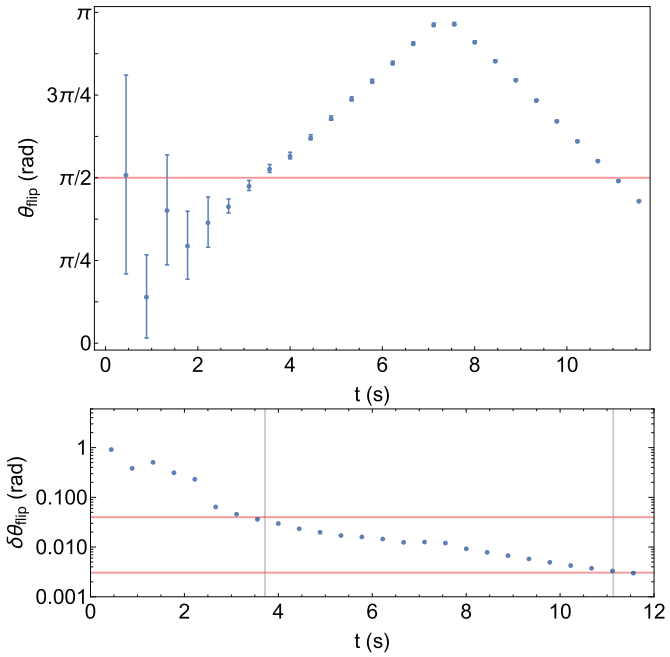

Fig. 11. Calculated flip angles θ_{flip} (upper plot) and their uncertainties $\delta\theta_{\text{flip}}$ (lower plot) as a function of the measurement time. The data from all eight CsOPMs was used. The two times at which a $\pi/2$ flip is achieved are shown as vertical lines. The horizontal lines in the lower figure mark the uncertainty of the θ_{flip} determination for the first and second occurence of a $\pi/2$ flip.

Table 3. Times at which a flip of the ^{3}He magnetization by $\theta_{\text{flip}} = +\pi/2$ (first occurrence) and $\theta_{\text{flip}} = -\pi/2$ (second occurrence) is reached.

CsOPM	$t_{+\pi/2}(s)$	$t_{-\pi/2}(s)$
Cs1	3.71(1)	11.13(2)
Cs3	3.73(1)	11.16(2)
Cs6	3.71(1)	11.12(3)
Cs8	3.69(2)	11.07(6)
Cs2	3.71(2)	11.11(6)
Cs4	3.71(1)	11.11(3)
Cs5	3.71(1)	11.12(3)
Cs7	3.70(2)	11.10(6)
Mean	3.713(3)	11.129(10)

and

$$t_{-\pi/2} = -\frac{\arccos(-\delta\omega^2/\omega_1^2) + 2\pi}{\Omega} \quad \text{for } \theta_{\text{flip}} = -\pi/2, \tag{18}$$

respectively. Table 3 gives predictions for the $t_{+\pi/2}$ and $t_{-\pi/2}$ flip-times based on the analysis of the individual CsOPMs' signals. The errors of the calculated Rabi frequencies and flip times are strongly dominated by the uncertainties of the B_1 estimation, uncertainties of the $\omega_{\text{L,He}}$ parameter playing a negligible role.

7 Conclusion

We have demonstrated a consistent way of interpreting measurements of the time dependent magnetic field created by a sample of nuclear spin-polarized ^{3}He during a spin-flip initiated by an external oscillating magnetic field. Our model allows us fitting these data and inferring – from the fit results – the effective Rabi frequency, thus a relation between the flipping time and the flip angle of the ^{3}He spin can be established. The method is a convenient means for measuring and controlling the spin-flip angle in experiments using ^{3}He/Cs magnetometers and requires only a coarse knowledge of the applied (static and oscillating) magnetic fields. In such an experiment one would typically perform a (long) Rabi nutation measurement and analyze it along the lines demonstrated above in order to characterize the system parameters. Assuming that the magnetic environment does not change with time, this knowledge can be used to calculate the flipping time needed to achieve any flip angle desired for the experiment. Moreover, the data recorded during the flipping used to prepare the ^{3}He for an actual experimental run can be used a posteriori to check whether the desired flip angle was really achieved. In this context our analysis suggests that it might be beneficial to do a $-\pi/2$ flip rather than a $+\pi/2$ because of the improved precision of the θ_{flip} determination for longer measurement times. The technique will be most profitable for the accurate monitoring of the static magnetic field in experimental searches for an nEDM. Our results show that measurements of the flip angle at a precision level of $\sim$4 mrad, sufficient for the nEDM application are feasible. Even better results, e.g., a scaling of the uncertainties with $1/\sqrt{n_{\text{Cs}}}$ can be expected by deploying an increased number n_{Cs} of readout CsOPMs. Our method further provides access to the ^{3}He's degree of spin polarization P_{He}. With a mechanically improved apparatus a polarization measurement with uncertainty below 1% seems feasible.

The described work was only made possible by the outstanding support from the mechanical workshops of the Physics Department at the University of Fribourg and the University of Mainz. We thank PTB for giving us access to their facilities and for the excellent technical support during the data recording. This work was supported by grants from the Deutsche Forschungsgemeinschaft (HE2308/14-1) and the Swiss National Science Foundation (200020_140421).

Author contribution statement

A. Weis, Z. D. Grujić, G. Bison, P. Knowles, M. Kasprzak and W. Heil were involved in the conceptual planing and construction of the device and in the development of data acquisition methods. Z.D. Grujić, P. Knowles, G. Bison, A. Schnabel and J. Voigt contributed to the data taking at PTB. A. Weis, Z.D. Grujić, G. Bison and W. Heil participated in the data analysis and the discussion of the results. A. Weis made strong contributions to the preparation of the manuscript. A. Kraft, A. Pazgalev, Z.D. Grujić, P. Knowles and M. Kasprzak contributed to important

precursor measurements at Johannes Gutenberg University Mainz. The studies presented in this paper are an extension of the Ph.D. thesis of H.-C. Koch who was leading all aspects of the investigations, data analysis and manuscript writing.

References

1. W. Heil, C. Gemmel, S. Karpuk, Y. Sobolev, K. Tullney, F. Allmendinger, U. Schmidt, M. Burghoff, W. Kilian, S. Knappe-Grüneberg et al., Ann. Phys. **525**, 539 (2013)
2. J. Grange, V. Guarino, P. Winter, K. Wood, H. Zhao, R.M. Carey, D. Gastler, E. Hazen, N. Kinnaird, J.P. Miller et al., Muon (g-2) Technical Design Report, arXiv:1501.06858 [physics.ins-det], January 2015
3. P.J. Mohr, B.N. Taylor, D.B. Newell, J. Phys. Chem. Ref. Data **41**, 043109 (2012)
4. A. Nikiel, P. Blümler, W. Heil, M. Hehn, S. Karpuk, A. Maul, E. Otten, L.M. Schreiber, M. Therekov, Eur. Phys. J. D **68**, 330 (2014)
5. G. Bevilacqua, V. Biancalana, Y. Dancheva, L. Moi, *Ann. R. NMR S* (Academic Press, 2013), Vol. 78 (Chapter 3)
6. J.M. Pendlebury, S. Afach, N.J. Ayres, C.A. Baker, G. Ban, G. Bison, K. Bodek, M. Burghoff, P. Geltenbort, K. Green, W.C. Griffith, M. van der Grinten, Z.D. Grujić, P.G Harris, V. Hélaine, P. Iaydjiev, S.N. Ivanov, M. Kasprzak, Y. Kermaidic, K. Kirch, H.-C. Koch, S. Komposch, A. Kozela, J. Krempel, B. Lauss, T. Lefort, Y. Lemière, D.J.R. May, M. Musgrave, O. Naviliat-Cuncic, F.M. Piegsa, G. Pignol, P.N. Prashanth, G. Quéméner, M. Rawlik, D. Rebreyend, J.D. Richardson, D. Ries, S. Roccia, D. Rozpedzik, A. Schnabel, P. Schmidt-Wellenburg, N. Severijns, D. Shiers, J.A. Thorne, A. Weis, O.J. Winston, E. Wursten, J. Zejma, G. Zsigmond, Phys. Rev. D **92**, 092003 (2015)
7. I. Altarev, G. Ban, G. Bison, K. Bodek, M. Burghoff, Z. Chowdhuri, M. Daum, C. Düsing, M. Fertl, P. Fierlinger, B. Franke, C. Grab, E. Gutsmiedl, G. Hampel, W. Heil, R. Henneck, M. Horras, N. Khomutov, K. Kirch, S. Kistryn, S. Knappe-Grüneberg, A. Knecht, P. Knowles, A. Kozela, A. Kraft, F. Kuchler, J.V. Kratz, T. Lauer, B. Lauss, T. Lefort, Y. Lemière, A. Mtchedlishvili, O. Naviliat-Cuncic, G. Quéméner, S. Paul, A.S. Pazgalev, G. Petzoldt, C. Plonka-Spehr, E. Pierre, G. Pignol, D. Rebreyend, S. Roccia, G. Rogel, P. Schmidt-Wellenburg, A. Schnabel, N. Severijns, Yu. Sobolev, R. Stoepler, A. Weis, N. Wiehl, J. Zejma, J. Zenner, G. Zsigmond, Nucl. Phys. A **844**, 47c (2010)
8. H.-C. Koch, G. Bison, Z.D. Grujić, W. Heil, M. Kasprzak, P. Knowles, A. Kraft, A. Pazgalev, A. Schnabel, J. Voigt, A. Weis, Eur. Phys. J. D **69**, 202 (2015)
9. C. Radhakrishna Rao, Bull. Calcutta Math. Soc. **37**, 81 (1945)
10. H.-C. Koch, G. Bison, Z.D. Grujić, W. Heil, M. Kasprzak, P. Knowles, A. Kraft, A. Pazgalev, A. Schnabel, J. Voigt, A. Weis, Eur. Phys. J. D **69**, 262 (2015)
11. P.J. Nacher, M. Leduc, J. Phys. **46**, 2057 (1985)
12. A. Kraft, H.-C. Koch, M. Daum, W. Heil, Th. Lauer, D. Neumann, A. Pazgalev, Yu. Sobolev, A. Weis, EPJ Tech. Instrum. **1**, 1 (2014)
13. K. Lenz, Test eines ^{3}He magnetometers für ein nedm experiment am PSI, Diplomarbeit, Johannes Gutenberg-Universitaet Mainz, 2009
14. S. Groeger, G. Bison, P.E. Knowles, R. Wynands, A. Weis, Sens. Actuators A: Phys. **129**, 1 (2006)
15. G. Bevilacqua, V. Biancalana, P. Chessa, Y. Dancheva, Appl. Phys. B **122**, 1 (2016)
16. N. Castagna, G. Bison, G. Domenico, A. Hofer, P. Knowles, C. Macchione, H. Saudan, A. Weis, Appl. Phys. B **96**, 763 (2009)
17. I. Hilschenz, D. Gutkelch, S. Hartwig, N. Höfner, R. Körber, H.J. Scheer, J. Voigt, M. Burghoff, L. Trahms, Biomed. Tech. **55**, 227 (2010)
18. J.D. Jackson, in *Classical electrodynamics* (Wiley, New York, 1962), Vol. 3
19. H.-C. Koch, An absolute combined ^{3}He/Cs magnetometer with fT sensitivity for the nEDM experiment at PSI, PhD thesis, Johannes Gutenberg-Universitaet Mainz and University of Fribourg, 2015